

pubsiacs.org/Nanol ett Letter

Highly Responsive Plasmon Modulation in Dopant-Segregated **Nanocrystals**

Bharat Tandon, Stephen L. Gibbs, Christopher Dean, and Delia J. Milliron*



Cite This: Nano Lett. 2023, 23, 908-915



Read Online

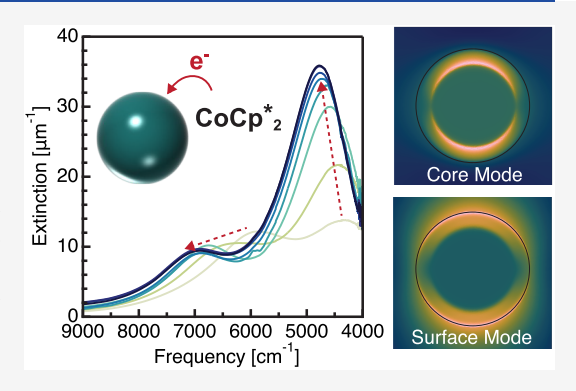
ACCESS I

Metrics & More

Article Recommendations

Supporting Information

ABSTRACT: Electron transfer to and from metal oxide nanocrystals (NCs) modulates their infrared localized surface plasmon resonance (LSPR), revealing fundamental aspects of their photophysics and enabling dynamic optical applications. We synthesized and chemically reduced dopantsegregated Sn-doped In₂O₃ NCs, investigating the influence of radial dopant segregation on LSPR modulation and near-field enhancement (NFE). We found that core-doped NCs show large LSPR shifts and NFE change during chemical titration, enabling broadband modulation in LSPR energy of over 1000 cm⁻¹ and of peak extinction over 300%. Simulations reveal that the evolution of the LSPR spectra during chemical reduction results from raising the surface Fermi level and increasing the donor defect density in the shell region. These results establish dopant segregation as a useful strategy to engineer the dynamic optical modulation in plasmonic semiconductor NC



heterostructures going beyond what is possible with conventional plasmonic metals.

KEYWORDS: metal oxide nanocrystals, localized surface plasmon resonance, chemical modulation, doping, near-field enhancement, indium tin oxide

egenerately doped semiconductor nanocrystals (NCs), particularly doped metal oxide NCs, have received considerable interest for their tunable localized surface plasmon resonance (LSPR) in the near- to mid-infrared region of the spectrum.1-4 LSPR, a coherent oscillation of the electron density driven by incident radiation, concentrates electromagnetic radiation around and between nanoparticles, which has been shown to be useful for photovoltaics, 5,6 photothermal therapy, 7,8 sensing, 9,10 surface-enhanced infrared spectroscopy, 11-13 and more. Furthermore, the change in LSPR absorption due to postsynthetic modulation of electronic charge in metal oxide NCs enables electrochromic smart windows 14-18 and redox sensing. 19-23 The potential of doped metal oxide NCs for such applications depends on the near-field enhancement (NFE), which quantifies the intensity by which light is concentrated near the NC surface, and on the dynamic range of LSPR modulation.

In Sn-doped In₂O₃ (Sn:In₂O₃) NCs, a prototypical doped metal oxide material, both NFE and LSPR modulation are strongly impacted by the presence of electron-deficient depletion layers in the near-surface region. 16,24,25 Within the depletion layer, the energy bands bend upward due to surface Fermi level pinning, and the free electron concentration is relatively low.²⁶ Consequently, the depletion layer reduces refractive index sensitivity,^{24,27} lowers the LSPR energy, extinction cross-section, and NFE, 28 and lessens conductivity in NC films.²⁹ However, a wide depletion layer can be beneficial for dynamic modulation of LSPR in electrochromic

or dynamic sensing applications because it increases the volume of the active material that can be capacitively charged and discharged.^{25,30} Maximal shifts in the LSPR energy are observed when electrons are added to or removed from NCs with low dopant concentrations that reduce the curvature of the bands and increase depletion width.²⁴ The depletion width can be tuned selectively for a given overall dopant concentration by varying the radial distributions of dopants with shell-doped NCs exhibiting a smaller depletion width than NCs with uniform or core-segregated doping.²⁹ The compression of the depletion width by tuning dopant placement strongly affects the sensitivity of the LSPR energy to changes in the solvent refractive index, 27 suggesting the highest NFE occurs for shell-doped NCs. Given the indications that surface depletion greatly impacts LSPR modulation of NCs with spatially uniform dopant concentrations, 23,24,31 we expected that the radial distribution of dopants may also substantially affect the dynamic range for LSPR energy, extinction, and NFE modulation upon reduction and oxidation of the NCs.

Received: October 26, 2022 Revised: January 10, 2023 Published: January 19, 2023





Radial segregation of dopants not only modifies the depletion layer near the NC surface but also drives band bending at the buried interface between doped and undoped regions. This double band bending has been simulated previously^{25,29} and has been shown experimentally to promote two peaks in the LSPR spectra of core/shell Sn:In2O3 NC heterostructures.²⁷ We hypothesized that by engineering the band bending in the depletion layer through dopant segregation, we could expand the range of dynamic modulation of LSPR. This investigation can provide a model for predicting postsynthetic changes in complex plasmonic systems where dual plasmon peaks are observed either due to heterostructure formation (metal/metal or metal/doped semiconductor)^{32–37} or anisotropy.³⁸⁻⁴¹ Moreover, the implications of surface depletion in manipulating the distribution of charge carriers within the NCs can be implemented in semiconductor heterostructures beyond plasmonics, for example, those based on GaAs/(Ga,Al)As. 42,43

By monitoring the changing LSPR absorption while postsynthetically reducing solvent-dispersed NCs, 30,44,45 we investigated the influence of dopant radial distribution on spectral modulation and NFE of core-shell Sn:In2O3 NCs of the same size but with different dopant placements. We found that dopant segregation to either the core or the shell has a profound influence on the extent of LSPR modulation, allowing the realization of broadband modulation of LSPR energy over 1000 cm⁻¹ and of peak extinction over 300% in core-doped NCs. Through simulations, we demonstrate the ability to track nanometer-scale changes in the intra-NC electron density profiles based on benchtop, ensemble measurements. These insights allow us to determine that surface Fermi level and the donor defect concentration in the shell region are responsible factors driving the spectral changes during chemical titration, providing a new understanding of the electronic changes that occur during postsynthetic doping. Furthermore, simulating the NFE through the reduction process revealed that core-doped NCs exhibit a greater change in both the maximum intensity and decay length of the NFE away from the NC surface than shell-doped NCs. This study illustrates how dopant modulation and depletion layer engineering can create semiconductor NC heterostructures to control the band profile to engineer not only the static but also the dynamic plasmonic response.

To precisely control dopant incorporation and NC size, we employed slow-injection syntheses and purified NC cores before shell overgrowth to minimize compositional gradations and create abrupt compositional heterojunctions. 26-28,46-48 Since the volume fraction of the depletion layer and its impact on LSPR are sensitive to changes in NC diameter, we fixed the overall diameter of the Sn:In2O3 NCs at about 24 nm while varying the dopant radial distribution. A summary of the synthesized NCs, including their average overall and core diameters obtained from bright-field scanning transmission electron microscopy (STEM), is provided in Table 1. The sample codes are assigned as "CD", "SD", or "UD", indicating whether the dopants are segregated in the core, the shell, or uniformly throughout the NC, respectively. Because all NCs were near 24 nm in overall diameter, the two-digit number at the end of the sample code represents the approximate size of the core. For instance, CD16 refers to a NC sample in which dopants are segregated in a 16 nm core with an approximately 4 nm thick undoped In_2O_3 shell.

Table 1. Experimentally Observed Physical Characteristics of Synthesized Sn:In₂O₃ NCs

Sample Code	Core Diameter [nm]	Overall Diameter [nm]	Shell Thickness [nm]	at% Sn by ICP-AES	at% Sn by XPS
CD16	16.7 ± 1.4	24.4 ± 2.2	3.9 ± 2.6	1.6	0.5
CD18	17.9 ± 1.7	24.7 ± 1.2	3.4 ± 2.1	2.1	0.6
CD20	20.8 ± 2.7	28.9 ± 3.3	4.1 ± 4.3	2.1	0.7
UD24	_	23.8 ± 1.8	_	8.3	10.4
SD18	18.4 ± 2.3	25.0 ± 2.1	3.3 ± 3.1	3.5	6.1
SD16	16.9 ± 1.4	23.6 ± 2.2	3.4 ± 2.6	4.3	7.9
SD14	13.5 ± 2.1	24.4 ± 2.2	5.5 ± 3.0	5.9	9.8

All NCs made from their constituent cores (Figures S1 and S2 in the Supporting Information) have a nearly spherical morphology with an average diameter of about 24 nm (with the notable exception of CD20) and low polydispersity (Figures 1a-c, S3, and S4). To evaluate the radial distribution

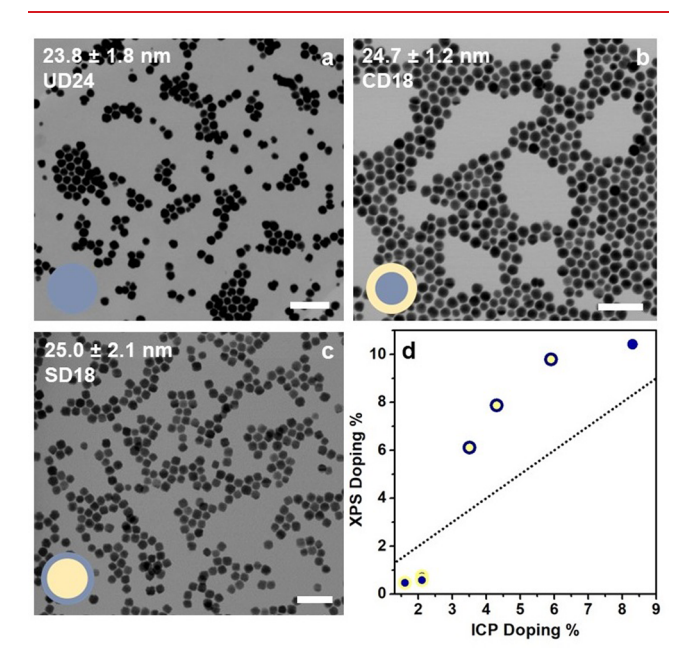


Figure 1. (a–c) STEM images of different core–shell-doped $\rm Sn:In_2O_3$ NCs depicting a spherical morphology and an average diameter of ${\sim}24$ nm for all samples. All scale bars are 100 nm. (d) A comparison of the overall doping percentage (obtained from ICP-AES) with the near-surface doping percentage (obtained from XPS) reveals the extent of dopant segregation in different core–shell $\rm Sn:In_2O_3$ NCs.

of dopants, we compare the near-surface Sn doping percentages obtained from X-ray photoelectron spectroscopy (XPS) with the overall Sn doping percentages acquired from inductively coupled plasma atomic emission spectroscopy (ICP-AES) (Figure 1d and Table 1). As expected from the synthesis, NCs with dopants segregated in the core (shell) display a much lower (higher) XPS doping % (XPS fittings in Figure S5) compared to the overall doping percentage obtained from ICP-AES. Core-doped NCs display a near-surface doping percentage almost one-third of the overall doping concentration, whereas the shell-doped NCs display a near-surface doping percentage almost twice the ICP-AES doping percentage.

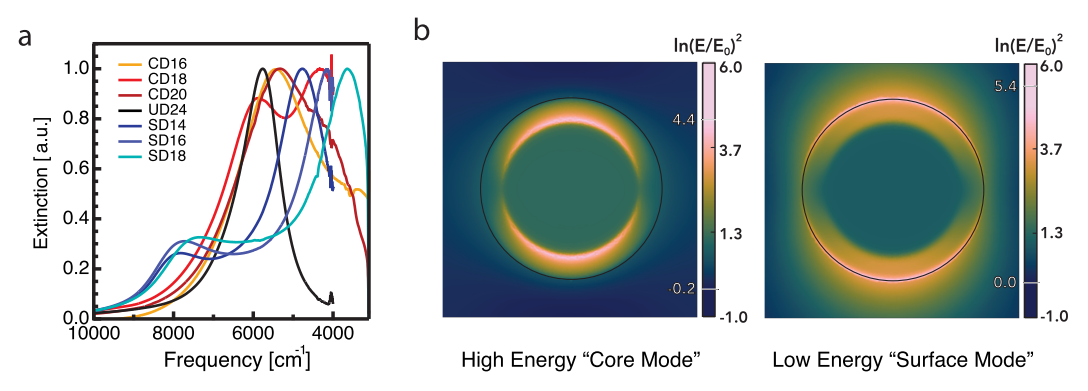


Figure 2. (a) Extinction spectra of different core—shell Sn:In₂O₃ NCs. (b) NFE maps for a core-doped particle with a Fermi level of 2.4 eV (relative to the center of the band gap) under excitation near the high energy "core mode" (left) and low energy "surface mode" (right). Numbers marked in white represent the maximum and minimum value of NFE.

Dopant segregation creates a contrast in the electrostatic potential that establishes an electron concentration difference within the shell and the core regions. Consequently, the NCs contain an undoped region with a low electron concentration and a doped region with a high electron concentration. This metallic core/metallic shell structure has been shown to give rise to dual-mode plasmonic absorption.²⁷ As expected, all the NCs belonging to the CD and SD series exhibit dual-mode LSPR spectra in contrast to the uniformly doped sample (UD24) that displays a single plasmonic peak (Figure 2a). These two LSPR modes originate from two distinct dielectric interfaces (core/shell and shell/surface) as depicted by the NFE maps in Figure 2b. For simplicity, we will refer to the high-energy LSPR mode as the "core" mode and the lowenergy LSPR mode as the "surface" mode throughout the manuscript.

Aiming to understand how these differences in the radial distribution of dopants and electrons impact the modulation of LSPR, we performed chemical titrations on all NCs using a reducing agent, decamethylcobaltocene (CoCp₂*). To perform these chemical reduction experiments, NCs were dispersed in a toluene:tetrahydrofuran (1:1 volume ratio) mixture anaerobically, and 50 μ L of 0.005 M [H(OEt)₂]⁺[BAr₄F]⁻ (also known as Brookhart's acid) in THF was subsequently added. Thereafter, 5 μ L aliquots of 0.005 M CoCp₂* solution in toluene were added to the NC dispersion while extinction spectra were collected continuously (see the experimental section in the SI for details).

Prior work found that volumetric addition of $CoCp_2^*$ to NC dispersions increases both the LSPR energy and extinction for uniformly doped $Sn:In_2O_3$ $NCs.^{30}$ The LSPR energy and extinction increase until a saturation point, and they decrease gradually after that, suggesting the transfer of electrons from $CoCp_2^*$ to the NCs (Figure 3a) until a thermodynamic limit is reached and a decrease in the colloidal stability past saturation, respectively. Quite expectedly, chemical reduction of the uniformly doped NCs (UD24) follows this behavior (Figure S6).

NCs with spatially segregated dopants exhibit distinct spectral evolution during reduction. Though shell-doped (Figures 3b and S7) and core-doped (Figure 3c) NCs both exhibit two spectral modes throughout, the core and surface modes respond differently to reduction for the two types of heterostructures. With the addition of CoCp₂*, there is a gradual increase in the LSPR energy and extinction of both the core and surface modes for all shell-doped samples. These

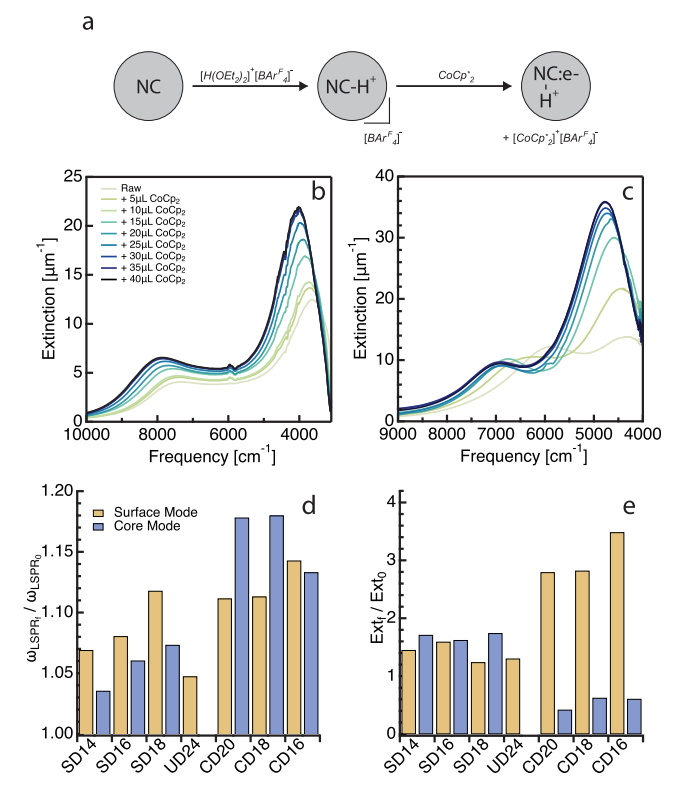


Figure 3. (a) Chemical equation depicting the mechanism of electron transfer from $CoCp_2^*$ to NC. Trends in infrared plasmonic modulation, with examples of series of spectra during reductive titration for (b) SD18 and (c) CD18. Relative change in (d) peak position and (e) extinction upon reduction.

changes are intuitive, since an increase in the electron concentration is expected to increase both the LSPR energy and extinction. To track the peak positions and intensities, we fit the spectra to a summation of two plasmonic peaks (Figure S8) and plotted the ratios of the post-titration peak positions to the pretitration peak positions (Figure 3d). We did the same for the peak extinction (Figure 3e). Interestingly, for all samples in the SD series, the energy difference between the core and surface modes ($\Delta\omega_{split}$) is not affected significantly by the chemical reduction (Table 2), no matter the shell thickness. However, the extent of the LSPR shift (for both core and surface modes) increases for thinner Sn:In₂O₃ shells (from SD14 to SD18), as depicted in Table 2 and Figure 3d. Since the extent of LSPR peak shifting is governed by

Table 2. Determining the Maximum Shift in the LSPR Frequency of Different Sn:In₂O₃ NCs after Reducing with CoCp₂**a

Sample Code	$\omega_{hi,i}~[\mathrm{cm}^{-1}]$	$\omega_{lo,i}~[\mathrm{cm}^{-1}]$	$\omega_{hi\!,\!f}~[\mathrm{cm}^{-1}]$	$\omega_{lof} [m cm^{-1}]$	$\Delta\omega_{hi}~[\mathrm{cm}^{-1}]$	$\Delta\omega_{lo}~[{ m cm}^{-1}]$	$\Delta\omega_{split,i}$ [cm ⁻¹]	$\Delta\omega_{split,f}[m cm^{-1}]$
CD16	5455	3685	6181	4211	726	526	1770	1970
CD18	5981	4296	7057	4782	1076	486	1685	2275
CD20	5516	4170	6499	4635	983	465	1346	1864
UD24	5811	-	6086	-	275	-	-	-
SD18	7070	3632	7588	4060	518	428	3438	3528
SD16	7491	4141	7943	4474	452	333	3550	3469
SD14	7764	4739	8039	5066	275	327	3025	2973

^aThe LSPR frequencies are shown for the core (surface) peak before, $\omega_{hi,i}$ ($\omega_{lo,i}$), and after, $\omega_{hi,j}$ ($\omega_{lo,j}$), chemical reduction. These values were obtained by deconvoluting the extinction spectra into individual LSPR peaks by fitting. $\Delta\omega_{hi}$ and $\Delta\omega_{lo}$ represent the maximal shifts in peak positions of the core and surface modes upon reduction, respectively. $\Delta\omega_{split,i}$ and $\Delta\omega_{split,j}$ represent the magnitudes of the peak splittings between the core and surface modes before and after reduction, respectively.

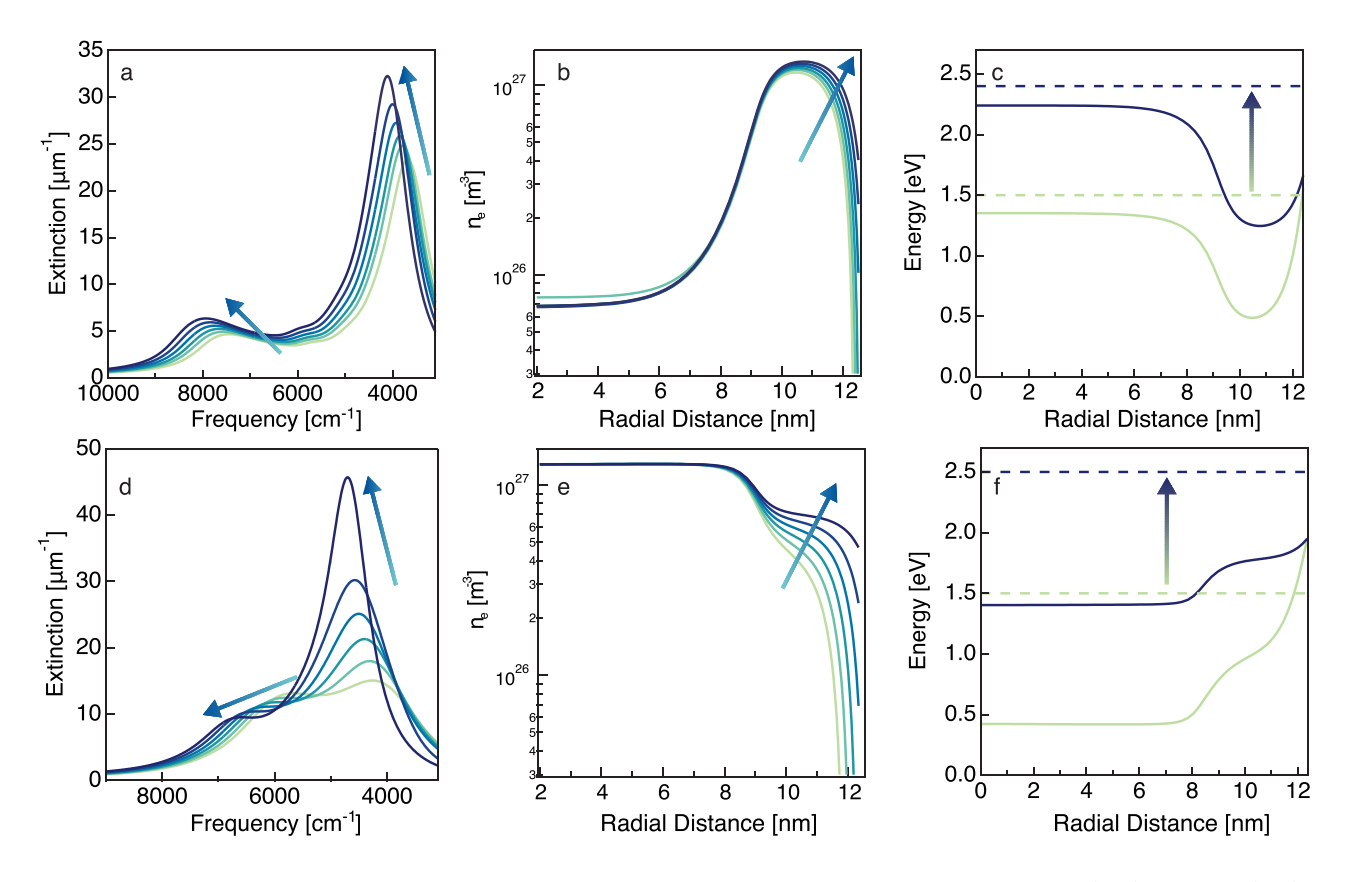


Figure 4. Simulated trends in plasmonic extinction, electron concentration, and conduction band edge energies for (a-c) SD18 and (d-f) CD18. The arrows indicate increasing reduction. Zero energy is set to the middle of the band-gap, and the band edge energy at the surface serves as a reference energy.

depletion effects in doped metal oxide NCs, it follows logically that an increase in the thickness of the doped shell which increases overall doping (increasing LSPR peak energy and reducing the depletion volume) leads to a systematic yet modest shift in the LSPR energy and extinction for the shell-doped series.

Increasing reduction by CoCp₂* induces a drastically different optical response for core-doped NCs (Figures 3c and S9). Both LSPR modes again increase in energy, but the shift of the core mode is much greater than that of the surface mode (Figure 3d and Table 2). The core mode is modulated by almost 1100 cm⁻¹, which is the largest modulation observed so far for Sn:In₂O₃ NCs—even larger than that observed for low-doped small-sized (8 nm 4.5% Sn doping) uniformly doped Sn:In₂O₃ NCs.³⁰ The drastic modulation is particularly

unexpected in NCs that are 8% doped in the core region (highly doped) and large in size (\sim 24 nm). While the stronger, surface mode is shifted more modestly, similar to the shifts found for shell-doped NCs, the extinction at this peak is greatly enhanced, by up to 300% by chemical reduction (Figure 3e). Conversely, for the core-doped series, the core mode decreases in extinction by nearly 2-fold while its energy increases (Figure 3d,e). A large LSPR shift paired with a decrease in extinction is counterintuitive because raising electron concentration usually increases both LSPR energy and extinction concomitantly. 24,28,30,49

To rationalize these differences in modulation behavior, we simulated the plasmonic absorption of NCs that were modeled in COMSOL to exactly resemble the size and doping distributions of our samples. We reliably reproduced both

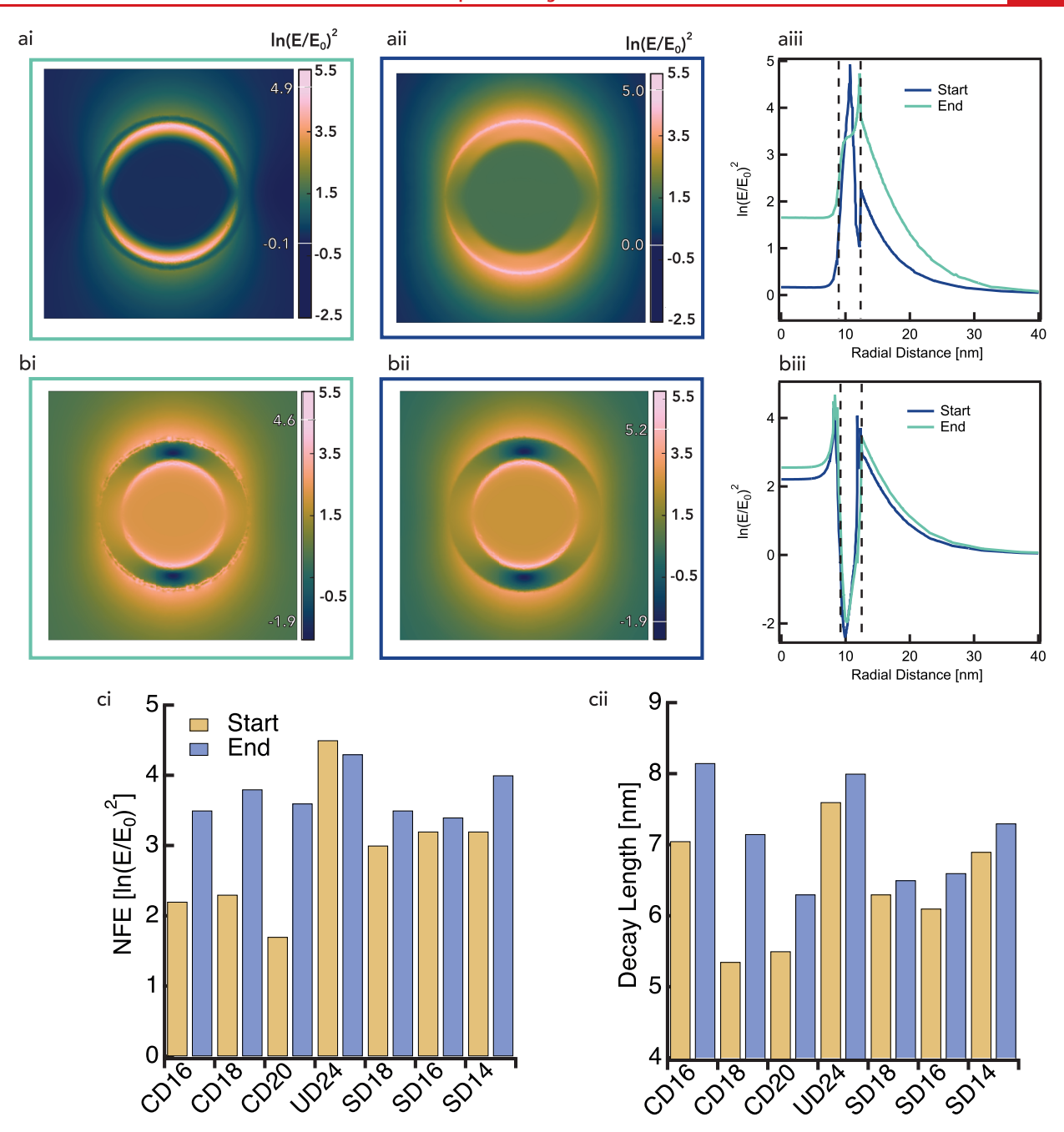


Figure 5. NFE maps for the surface mode for CD18 (ai) before and (aii) after reduction. NFE maps for the surface mode for SD18 (bi) before and (bii) after reduction. Vertical line scans for NFE maps of (aiii) CD18 and (biii) SD18. Simulated (ci) NFE at the NC surface and (cii) decay length across all samples.

LSPR energy and extinction trends of all dopant-segregated and uniform doping samples across all titrations (Figures S10–S12) by changing two physical parameters: (1) the Fermi level at the NC surface E_s and (2) the donor concentration in the shell (N_{shell}) (see Supplementary Text T1 for details). Changing only one of the parameters did not result in a satisfactory reproduction of both energy and extinction trends (Figures S13 and S14). We identified that these were the two key parameters after observing that the spectra could not be reproduced by varying other possible parameters such as the donor concentration in the core (N_{core}) or the refractive index of the surroundings (Figures S15 and S16). Prior work has shown that doping indium oxide with aliovalent donors adds free electrons while stabilizing, or lowering, the energy of the

conduction band.⁵⁰ In contrast, photodoping was shown to add electrons while raising the surface Fermi level, which must be equilibrated to the Fermi level in the NC core.⁵¹ Our results indicate that chemical titration by this method promotes both of these phenomena. In other work studying postsynthetic modulation of dopant-segregated $Sn:In_2O_3$ NCs, photodoping was shown to increase the electron density near the surface, but no effect on the surface Fermi level was reported.²⁵ These differences in the analysis may reflect underlying differences in charge compensation mechanisms. Our current data set also provides a more complete view of the evolution in spectral lineshapes than was available in the recent photodoping study; the additional information helps inform the analysis and reveals the importance of changes to both E_s and N_{shell} .

The changing spatial distribution of electrons, shaped by the band bending electrostatic landscape created by the surface Fermi level and donor concentration profile, is responsible for the evolving lineshapes of the plasmonic spectra during chemical reduction. This assessment holds for both shelland core-doped NCs, as exemplified by SD18 and CD18 (simulations shown in Figure 4), where the distribution of dopants determines the initial distribution of electrons and the subsequent modulation of that electron profile. For the shelldoped NCs, reduction broadens the thin shell of high electron concentration by progressively filling the near-surface depletion layer. The core-doped NCs contain a double band bending region as observed in prior work.²⁵ Reduction modulates the width and electron density in both band bending regions, effectively compressing the surface depletion layer and increasing the electron density in the optically active shell. Electron transfer from CoCp2* raises the Fermi level (Figure 4c,f). With increasing reduction, the electron concentration tends toward uniformity and the spectra tend toward a single peak of high energy and intensity. In the interim, the contribution of the optically active shell (whose presence promotes the core mode) trends toward subsuming the core mode peak, manifesting in the progressive disappearance of the core mode.

We initially expected that any one or any combination of four parameters $(N_{core}, N_{shell}, E_s)$, and refractive index of surroundings) could change throughout the course of reduction and impact the optical response. After sweeping through all parameters (Supplementary Text T2), we found that increasing N_{shell} and E_s with chemical reduction was the only combination that reproduced the LSPR energy and extinction trends in our data. In a sample set encompassing NCs of seven distinct dopant distributions, our simulations reliably reproduce the evolution of the plasmonic response through the course of titration. This broad-ranging efficacy in reproducing the experimental trends makes us confident that N_{shell} and E_s are the two primary physical parameters responsible for the spectral changes with increasing CoCp₂*. The ability of the simulations to consistently reproduce the absorption characteristics of different Sn:In₂O₃ NCs through a spherical approximation makes it evident that slight deviation from spherical geometry has no profound effect on the LSPR absorption. The initial and final values of these parameters, where simulations were found to approximate the experimental spectra, are listed in Table S1 along with the change in the number of electrons (i.e., electrons stored) per NC. Comparison of the parameters makes it evident that there is a greater change in N_{shell} and E_s in core-doped NCs vs shelldoped or uniformly doped Sn:In2O3 NCs, which translates to a broader modulation of LSPR energy and extinction for coredoped Sn: In_2O_3 NCs. The magnitude of change in E_s with chemical reduction is in accordance with expected values from literature reports. 45,50,52 Further, the number of electrons stored is consistent among most samples with the large size of NCs allowing them to add a high number of electrons,⁴⁵ indicating that it is the spatial location, not the quantity, of electrons stored that strongly affects the optical response.

Lastly, our simulations also enable mapping of the enhanced electric field, which offers an additional lens through which to view the advantage of increased plasmonic modulation in coredoped samples. The magnitude and spatial extent of the NFE are central to enhanced sensing and detection and to enhancing light absorption or emission for energy conversion.

We mapped the NFE at the peak of both the core and surface modes for all samples, both before and after reduction (Figures S17-S23). We found that the increased modulation in absorption also manifests in an increase in the modulation of NFE. As an example, we plot the NFE maps and vertical line scans of those maps for CD18 and SD18 (Figure 5ai-aiii and bi-biii). Apparently, the NFE around the NC extends much further with reduction in CD18 than SD18 (Figure 5ai,aii and bi,bii). To evaluate the sensitivity of the LSPR to the surroundings, two aspects of the NFE can be considered: (1) the magnitude near the NC surface and (2) the spatial extent of NFE in the surrounding area. We investigated these two metrics for the more intense, low energy peaks of each sample by taking vertical line scans of the NFE maps (Figure 5aiii,biii) and recording the NFE at the surface and the decay length (distance from the NC surface at which the NFE diminishes to 1/e times the value at the surface).

The magnitude of the NFE at the surface and its decay length are modulated significantly more in CD18 than in SD18. For all core- and shell-doped NCs, chemical reduction causes a change in decay length behavior for core and surface peaks, which is attributed to a modification in electron distribution after chemical reduction (Figure 5ci,cii). On average, the core-doped NCs increase in NFE and decay length by 21 and 79%, respectively, while for shell-doped NCs these parameters increase by only 6 and 16%, respectively. Although the NFE at the surface is consistently higher for shell-doped samples before reduction, the core-doped samples have a comparable NFE after reduction. The same holds for the decay length, and in fact, the largest decay length we found was about 8 nm in CD16, after reduction (Figures S24 and S25). A decrease in surface depletion due to chemical reduction increases the plasmonic volume and electron concentration in the shell thus increasing NFE and decay length. This increase indicates that the enhanced electric field under LSPR excitation can influence the photophysical properties of adjacent molecules and materials in a larger surrounding region, and stronger coupling can be anticipated between neighboring NCs in an assembly.

In conclusion, by leveraging the flexibility of the continuous growth procedure, we synthesized core/shell Sn:In₂O₃ NCs of similar sizes but different dopant distributions (core, shell, or uniformly doped). Due to the presence of two distinct regions of the electron concentration, the dopant-segregated core/shell Sn:In2O3 NCs exhibited dual plasmon peaks while the uniformly doped NCs exhibited only a single plasmon peak. By employing CoCp2* as a reducing agent, we investigated the effect of postsynthetic doping on two electronic interfaces simultaneously and learned that dopant segregation drastically impacts the extent of LSPR modulation. While shell-doped NCs displayed a modest modulation of LSPR energy and extinction in both plasmonic peaks, core-doped NCs exhibited broadband modulation of both LSPR energy (~1100 cm⁻¹) and extinction (over 300% enhancement). The large shifts we observed bring the reduced NCs well within the NIR window for applications in photothermal therapy, 7,8 electrochromics, and photovoltaics. 53 These shifts result from extensive electron storage in the NCs. Simulations suggest these electrons are compensated partly by increasing the donor density in the shell region, and they bring about a significant increase in the surface Fermi energy. Through analysis of near-field intensity maps, we discovered that during the reduction process, the near-field intensity in core-doped NCs grows to a larger extent

and extends farther in space than for shell-doped NCs. With such strong and spatially extensive regions of NFE, the reduced core-doped NCs are attractive candidates for dynamic sensing, surface-enhanced infrared absorption, and other near-field applications where modulation or postsynthetic tuning may be advantageous. More broadly, dopant segregation is a powerful tool to achieve depletion layer engineering in heterostructured NCs and may facilitate the design of new optical phenomena in other depletion layer engineered semiconductor heterostructures or those based on other heterostructures like silica/Au core/shell nanocrystals³⁴ and modulation-doped GaAs/(AI,Ga)As.⁴²

ASSOCIATED CONTENT

Supporting Information

The Supporting Information is available free of charge at https://pubs.acs.org/doi/10.1021/acs.nanolett.2c04199.

Synthetic protocol, equipment and characterization technique specifications, STEM, chemical titration spectra of samples not shown in the manuscript, discussion of COMSOL simulation model, fitting plots and results for shell-doped and core-doped series, fitting plots and simulations of the electronic profiles and absorption spectra of different Sn:In₂O₃ NCs, constraints for fit parameters, and NFE maps and line scans and parameters obtained thereafter (PDF)

AUTHOR INFORMATION

Corresponding Author

Delia J. Milliron — McKetta Department of Chemical Engineering, University of Texas at Austin, Austin, Texas 78712, United States; Orcid.org/0000-0002-8737-451X; Email: milliron@che.utexas.edu

Authors

Bharat Tandon – McKetta Department of Chemical Engineering, University of Texas at Austin, Austin, Texas 78712, United States; Oorcid.org/0000-0003-1108-9859

Stephen L. Gibbs – McKetta Department of Chemical Engineering, University of Texas at Austin, Austin, Texas 78712, United States; Oorcid.org/0000-0003-2533-0957

Christopher Dean – McKetta Department of Chemical Engineering, University of Texas at Austin, Austin, Texas 78712, United States

Complete contact information is available at: https://pubs.acs.org/10.1021/acs.nanolett.2c04199

Author Contributions

B.T., S.L.G, and C.D. contributed equally to the manuscript.

The authors declare no competing financial interest.

ACKNOWLEDGMENTS

This research was supported by the National Science Foundation (CHE-1905263), including a Graduate Research Fellowship under Award Number (DGE-1610403, S.L.G.) with additional support from the Welch Foundation (F-1848).

REFERENCES

(1) Willets, K. A.; Van Duyne, R. P. Localized Surface Plasmon Resonance Spectroscopy and Sensing. *Annu. Rev. Phys. Chem.* **2007**, 58, 267–297.

- (2) Tandon, B.; Ashok, A.; Nag, A. Colloidal transparent conducting oxide nanocrystals: A new infrared plasmonic material. *Pramana* **2015**, *84*, 1087–1098.
- (3) Agrawal, A.; Cho, S. H.; Zandi, O.; Ghosh, S.; Johns, R. W.; Milliron, D. J. Localized Surface Plasmon Resonance in Semi-conductor Nanocrystals. *Chem. Rev.* **2018**, *118*, 3121–3207.
- (4) Faucheaux, J. A.; Stanton, A. L. D.; Jain, P. K. Plasmon Resonances of Semiconductor Nanocrystals: Physical Principles and New Opportunities. *J. Phys. Chem. Lett.* **2014**, *5*, 976–985.
- (5) Atwater, H. A.; Polman, A. Plasmonics for Improved Photovoltaic Devices. *Nat. Mater.* **2010**, *9*, 205–213.
- (6) Zhou, D.; Li, X.; Zhou, Q.; Zhu, H. Infrared Driven Hot Electron Generation and Transfer from Non-noble Metal Plasmonic Nanocrystals. *Nat. Commun.* **2020**, *11*, 2944.
- (7) Kim, M.; Lee, J.-H.; Nam, J.-M. Plasmonic Photothermal Nanoparticles for Biomedical Applications. *Adv. Sci.* **2019**, *6*, 1900471.
- (8) Zhou, C.; Zhang, L.; Sun, T.; Zhang, Y.; Liu, Y.; Gong, M.; Xu, Z.; Du, M.; Liu, Y.; Liu, G.; Zhang, D. Activatable NIR-II Plasmonic Nanotheranostics for Efficient Photoacoustic Imaging and Photothermal Cancer Therapy. *Adv. Mater.* **2021**, *33*, 2006532.
- (9) Petryayeva, E.; Krull, U. J. Localized Surface Plasmon Resonance: Nanostructures, Bioassays and Biosensing—A Review. *Anal. Chim. Acta* **2011**, 706, 8–24.
- (10) Qu, J.; Livache, C.; Martinez, B.; Gréboval, C.; Chu, A.; Meriggio, E.; Ramade, J.; Cruguel, H.; Xu, X. Z.; Proust, A.; Volatron, F.; Cabailh, G.; Goubet, N.; Lhuillier, E. Transport in ITO Nanocrystals with Short- to Long-Wave Infrared Absorption for Heavy-Metal-Free Infrared Photodetection. ACS Appl. Nano Mater. 2019, 2, 1621–1630.
- (11) Chong, X.; Zhang, Y.; Li, E.; Kim, K.-J.; Ohodnicki, P. R.; Chang, C.-h.; Wang, A. X. Surface-Enhanced Infrared Absorption: Pushing the Frontier for On-Chip Gas Sensing. *ACS Sensors* **2018**, *3*, 230–238.
- (12) Agrawal, A.; Singh, A.; Yazdi, S.; Singh, A.; Ong, G. K.; Bustillo, K.; Johns, R. W.; Ringe, E.; Milliron, D. J. Resonant Coupling between Molecular Vibrations and Localized Surface Plasmon Resonance of Faceted Metal Oxide Nanocrystals. *Nano Lett.* **2017**, *17*, 2611–2620.
- (13) Zhu, Q.; Jiang, S.; Ye, K.; Hu, W.; Zhang, J.; Niu, X.; Lin, Y.; Chen, S.; Song, L.; Zhang, Q.; Jiang, J.; Luo, Y. Hydrogen-Doping-Induced Metal-Like Ultrahigh Free-Carrier Concentration in Metal-Oxide Material for Giant and Tunable Plasmon Resonance. *Adv. Mater.* **2020**, *32*, 2004059.
- (14) Garcia, G.; Buonsanti, R.; Runnerstrom, E. L.; Mendelsberg, R. J.; Llordes, A.; Anders, A.; Richardson, T. J.; Milliron, D. J. Dynamically Modulating the Surface Plasmon Resonance of Doped Semiconductor Nanocrystals. *Nano Lett.* **2011**, *11*, 4415–4420.
- (15) Llordés, A.; Garcia, G.; Gazquez, J.; Milliron, D. J. Tunable Near-Infrared and Visible-Light Transmittance in Nanocrystal-in-Glass Composites. *Nature* **2013**, *500*, 323.
- (16) Tandon, B.; Agrawal, A.; Heo, S.; Milliron, D. J. Competition between Depletion Effects and Coupling in the Plasmon Modulation of Doped Metal Oxide Nanocrystals. *Nano Lett.* **2019**, *19*, 2012–2019.
- (17) Runnerstrom, E. L.; Llordés, A.; Lounis, S. D.; Milliron, D. J. Nanostructured Electrochromic Smart Windows: Traditional Materials and NIR-selective Plasmonic Nanocrystals. *Chem. Commun.* **2014**, *50*, 10555–10572.
- (18) Zhang, S.; Li, Y.; Zhang, T.; Cao, S.; Yao, Q.; Lin, H.; Ye, H.; Fisher, A.; Lee, J. Y. Dual-Band Electrochromic Devices with a Transparent Conductive Capacitive Charge-Balancing Anode. ACS Appl. Mater. & Interfaces 2019, 11, 48062–48070.
- (19) Mendelsberg, R. J.; McBride, P. M.; Duong, J. T.; Bailey, M. J.; Llordes, A.; Milliron, D. J.; Helms, B. A. Dispersible lasmonic Doped Metal xide Nanocrystal Sensors that Optically Track Redox Reactions in Aqueous Media with Single-Electron Sensitivity. *Adv. Opt. Mater.* **2015**, *3*, 1293–1300.

- (20) Graham, A. J.; Gibbs, S. L.; Saez Cabezas, C. A.; Wang, Y.; Green, A. M.; Milliron, D. J.; Keitz, B. K. In Situ Optical Quantification of Extracellular Electron Transfer Using Plasmonic Metal Oxide Nanocrystals. *ChemElectroChem.* **2022**, 9, No. e202101423.
- (21) Zhang, C.; Jia, F.; Li, Z.; Huang, X.; Lu, G. Plasmon-Generated Hot Holes for Chemical Reactions. *Nano Res.* **2020**, *13*, 3183.
- (22) Li, J.; Lou, Z.; Li, B. Engineering Plasmonic Semiconductors for Enhanced Photocatalysis. *J. Mater. Chem. A* **2021**, *9*, 18818–18835.
- (23) Ghini, M.; Curreli, N.; Camellini, A.; Wang, M.; Asaithambi, A.; Kriegel, I. Photodoping of Metal Oxide Nanocrystals for Multi-charge Accumulation and Light-driven Energy Storage. *Nanoscale* **2021**, *13*, 8773–8783
- (24) Zandi, O.; Agrawal, A.; Shearer, A. B.; Reimnitz, L. C.; Dahlman, C. J.; Staller, C. M.; Milliron, D. J. Impacts of Surface Depletion on the Plasmonic Properties of Doped Semiconductor Nanocrystals. *Nat. Mater.* **2018**, *17*, 710–717.
- (25) Ghini, M.; Curreli, N.; Lodi, M. B.; Petrini, N.; Wang, M.; Prato, M.; Fanti, A.; Manna, L.; Kriegel, I. Control of Electronic Band Profiles through Depletion Layer Engineering in Core—shell Nanocrystals. *Nat. Commun.* **2022**, *13*, 537.
- (26) Gibbs, S. L.; Staller, C. M.; Milliron, D. J. Surface Depletion Layers in Plasmonic Metal Oxide Nanocrystals. *Acc. Chem. Res.* **2019**, 52, 2516–2524.
- (27) Gibbs, S. L.; Dean, C.; Saad, J.; Tandon, B.; Staller, C. M.; Agrawal, A.; Milliron, D. J. Dual-Mode Infrared Absorption by Segregating Dopants within Plasmonic Semiconductor Nanocrystals. *Nano Lett.* **2020**, *20*, 7498–7505.
- (28) Staller, C. M.; Gibbs, S. L.; Saez Cabezas, C. A.; Milliron, D. J. Quantitative Analysis of Extinction Coefficients of Tin-Doped Indium Oxide Nanocrystal Ensembles. *Nano Lett.* **2019**, *19*, 8149–8154.
- (29) Staller, C. M.; Robinson, Z. L.; Agrawal, A.; Gibbs, S. L.; Greenberg, B. L.; Lounis, S. D.; Kortshagen, U. R.; Milliron, D. J. Tuning Nanocrystal Surface Depletion by Controlling Dopant Distribution as a Route Toward Enhanced Film Conductivity. *Nano Lett.* **2018**, *18*, 2870–2878.
- (30) Tandon, B.; Shubert-Zuleta, S. A.; Milliron, D. J. Investigating the Role of Surface Depletion in Governing Electron-Transfer Events in Colloidal Plasmonic Nanocrystals. *Chem. Mater.* **2022**, *34*, 777–788.
- (31) Agrawal, A.; Kriegel, I.; Runnerstrom, E. L.; Scotognella, F.; Llords, A.; Milliron, D. J. Rationalizing the Impact of Surface Depletion on Electrochemical Modulation of Plasmon Resonance Absorption in Metal Oxide Nanocrystals. *ACS Photonics* **2018**, *5*, 2044–2050.
- (32) Link, S.; Wang, Z. L.; El-Sayed, M. A. Alloy Formation of Gold-Silver Nanoparticles and the Dependence of the Plasmon Absorption on Their Composition. *J. Phys. Chem. B* **1999**, *103*, 3529–3533.
- (33) Sun, M.; Fu, X.; Chen, K.; Wang, H. Dual-Plasmonic Gold@Copper Sulfide Core-Shell Nanoparticles: Phase-Selective Synthesis and Multimodal Photothermal and Photocatalytic Behaviors. ACS Appl. Mater. & Interfaces 2020, 12, 46146–46161.
- (34) Oldenburg, S.; Averitt, R.; Westcott, S.; Halas, N. Nanoengineering of Optical Resonances. *Chem. Phys. Lett.* **1998**, 288, 243–247.
- (35) Wang, H.; Brandl, D. W.; Nordlander, P.; Halas, N. J. Plasmonic Nanostructures: Artificial Molecules. *Acc. Chem. Res.* **2007**, 40, 53–62.
- (36) Tang, W.; Dong, Z.; Zhang, R.; Yi, X.; Yang, K.; Jin, M.; Yuan, C.; Xiao, Z.; Liu, Z.; Cheng, L. Multifunctional Two-Dimensional Core—Shell MXene@Gold Nanocomposites for Enhanced Photo—Radio Combined Therapy in the Second Biological Window. ACS Nano 2019, 13, 284—294.
- (37) Cai, R.; Xiang, H.; Yang, D.; Lin, K.-T.; Wu, Y.; Zhou, R.; Gu, Z.; Yan, L.; Zhao, Y.; Tan, W. Plasmonic AuPt@CuS Heterostructure with Enhanced Synergistic Efficacy for Radiophotothermal Therapy. *J. Am. Chem. Soc.* **2021**, *143*, 16113–16127.
- (38) Gordon, T. R.; Paik, T.; Klein, D. R.; Naik, G. V.; Caglayan, H.; Boltasseva, A.; Murray, C. B. Shape-Dependent Plasmonic Response

- and Directed Self-Assembly in a New Semiconductor Building Block, Indium-Doped Cadmium Oxide (ICO). *Nano Lett.* **2013**, *13*, 2857–2863.
- (39) Huang, X.; Neretina, S.; El-Sayed, M. A. Gold Nanorods: From Synthesis and Properties to Biological and Biomedical Applications. *Adv. Mater.* **2009**, *21*, 4880–4910.
- (40) Cheref, Y.; Lochon, F.; Daugas, L.; Cleret de Langavant, C.; Larquet, r.; Baron, A.; Gacoin, T.; Kim, J. Dual–Band LSPR of Tungsten Bronze Nanocrystals Tunable over NIR and SWIR Ranges. *Chem. Mater.* **2022**, *34*, 9795–9802.
- (41) Hsu, S.-W.; On, K.; Tao, A. R. Localized Surface Plasmon Resonances of Anisotropic Semiconductor Nanocrystals. *J. Am. Chem. Soc.* **2011**, *133*, 19072–19075.
- (42) Gossard, A. C. Modulation Doping of Semiconductor Heterostructures. *Molecular Beam Epitaxy and Heterostructures* **1985**, 499–531.
- (43) Wang, D.; Li, X.-B.; Sun, H.-B. Modulation Doping: A Strategy for 2D Materials Electronics. *Nano Lett.* **2021**, *21*, 6298–6303.
- (44) Valdez, C. N.; Braten, M.; Soria, A.; Gamelin, D. R.; Mayer, J. M. Effect of Protons on the Redox Chemistry of Colloidal Zinc Oxide Nanocrystals. *J. Am. Chem. Soc.* **2013**, *135*, 8492–8495.
- (45) Valdez, C. N.; Schimpf, A. M.; Gamelin, D. R.; Mayer, J. M. Proton-Controlled Reduction of ZnO Nanocrystals: Effects of Molecular Reductants, Cations, and Thermodynamic Limitations. *J. Am. Chem. Soc.* **2016**, *138*, 1377–1385.
- (46) Jansons, A. W.; Plummer, L. K.; Hutchison, J. E. Living Nanocrystals. *Chem. Mater.* **2017**, 29, 5415–5425.
- (47) Jansons, A. W.; Hutchison, J. E. Continuous Growth of Metal Oxide Nanocrystals: Enhanced Control of Nanocrystal Size and Radial Dopant Distribution. *ACS Nano* **2016**, *10*, 6942–6951.
- (48) Ito, D.; Yokoyama, S.; Zaikova, T.; Masuko, K.; Hutchison, J. E. Synthesis of Ligand-Stabilized Metal Oxide Nanocrystals and Epitaxial Core/Shell Nanocrystals via a Lower-Temperature Esterification Process. ACS Nano 2014, 8, 64–75.
- (49) Kanehara, M.; Koike, H.; Yoshinaga, T.; Teranishi, T. Indium Tin Oxide Nanoparticles with Compositionally Tunable Surface Plasmon Resonance Frequencies in the Near-IR Region. *J. Am. Chem. Soc.* **2009**, *131*, 17736–17737.
- (50) Araujo, J. J.; Brozek, C. K.; Liu, H.; Merkulova, A.; Li, X.; Gamelin, D. R. Tunable Band-Edge Potentials and Charge Storage in Colloidal Tin-Doped Indium Oxide (ITO) Nanocrystals. *ACS Nano* **2021**, *15*, 14116–14124.
- (51) Schimpf, A. M.; Lounis, S. D.; Runnerstrom, E. L.; Milliron, D. J.; Gamelin, D. R. Redox Chemistries and Plasmon Energies of Photodoped In₂O₃ and Sn-Doped In₂O₃ (ITO) Nanocrystals. *J. Am. Chem. Soc.* **2015**, *137*, 518–524.
- (52) Brozek, C. K.; Hartstein, K. H.; Gamelin, D. R. Potentiometric Titrations for Measuring the Capacitance of Colloidal Photodoped ZnO Nanocrystals. *J. Am. Chem. Soc.* **2016**, *138*, 10605–10610.
- (53) Olaimat, M. M.; Yousefi, L.; Ramahi, O. M. Using Plasmonics and Nanoparticles to Enhance the Efficiency of Solar Cells: Review of Latest Technologies. *J. Opt. Soc. Am. B* **2021**, *38*, *638*–651.